

Self-Supervised Representation Learning for Astronomical Images

MD ABUL HAYAT,^{1,2,*} GEORGE STEIN,^{2,3,*} PETER HARRINGTON,² ZARIJA LUKIĆ,² AND MUSTAFA MUSTAFA²

¹*University of Arkansas, Fayetteville, AR 72701*

²*Lawrence Berkeley National Laboratory, Berkeley, CA 94720*

³*Berkeley Center for Cosmological Physics, University of California, Berkeley, CA 94720*

Submitted to The Astrophysical Journal Letters

ABSTRACT

Sky surveys are the largest data generators in astronomy, making automated tools for extracting meaningful scientific information an absolute necessity. We show that, without the need for labels, self-supervised learning recovers representations of sky survey images that are semantically useful for a variety of scientific tasks. These representations can be directly used as features, or fine-tuned, to outperform supervised methods trained only on labeled data. We apply a contrastive learning framework on multi-band galaxy photometry from the Sloan Digital Sky Survey (SDSS), to learn image representations. We then use them for galaxy morphology classification, and fine-tune them for photometric redshift estimation, using labels from the Galaxy Zoo 2 dataset and SDSS spectroscopy. In both downstream tasks, using the same learned representations, we outperform the supervised state-of-the-art results, and we show that our approach can achieve the accuracy of supervised models while using 2-4 times fewer labels for training.

1. INTRODUCTION

Observing and imaging objects in the sky has been the main driver of the scientific discovery process in astronomy, because doing controlled experiments is not a viable option. The rapid advance of digital sky surveys in the 1990s, spearheaded by SDSS (Gunn et al. 1998, 2006), has rendered obsolete the approach of manual inspection of images by an expert. Instead, computational analysis methods are constantly being developed and applied (Ivezić et al. 2019a). Additionally, “citizen science” like the Galaxy Zoo¹ project (GZ, Lintott et al. 2008) plays an important role for tasks which are too complex to describe algorithmically, yet are heuristically quite comprehensible to humans, such as classification of galaxies based on their morphological types (Lintott et al. 2013). In recent years, machine learning methods have proven particularly useful for both classification and regression tasks (see Stein 2020 for a comprehensive list), but the majority of published works rely on

the quantity and quality of (manually assigned) image labels.

Serendipitous discovery of an ionization echo from a recently faded quasar (Lintott et al. 2009), and the cumbersome search for similar systems that followed (Keel et al. 2012), showcases other big data challenges. It demonstrates the need for methods which allow for the discovery of truly unusual and previously unseen objects, and also the need to perform semantic (or feature) similarity searches on images in situations when the number of labels is as low as one. In the near future, incoming sky surveys such as the Vera Rubin Observatory (Ivezić et al. 2019b), Euclid (Laureijs et al. 2011), Nancy Grace Roman Space Telescope (Spergel et al. 2013), or the Square Kilometer Array² will open yet another research epoch, where datasets are of sizes which completely overwhelm even the most ambitious citizen science concepts. It is fair to say that the vast majority of images from these observatories will never be seen by a human eye. Thus, the capability to organize images without labels and programmatically search for semantic similarity or for interesting outliers will be

mahayat@uark.edu, gstein@berkeley.edu, pharrington@lbl.gov,
zarija@lbl.gov, mmustafa@lbl.gov

* Equal contribution first authors.

¹ <https://www.zooniverse.org/projects/zookeeper/galaxy-zoo/>

² <https://www.skatelescope.org/>

essential to maximize the scientific output of these missions.

This capability is heavily dependent on image *representations* — low-dimensional mappings of images which preserve their inherent information. Finding good representations is crucial to scientific *downstream* tasks such as clustering and classification of images, but is often elusive, partly due to the difficulty of gathering enough high-quality labels. Unsupervised machine learning methods aim to learn semantically meaningful representations of the data without relying on any labels (see, e.g. Alloghani et al. 2020). Many such methods have already been applied to studies of galaxy morphology (Hocking et al. 2018; Martin et al. 2020; Cheng et al. 2020a; Spindler et al. 2020), identification of strong lenses (Cheng et al. 2020b), and anomaly detection (Xiong et al. 2018; Margalef-Bentabol et al. 2020). Unfortunately, across most computer vision applications, the utility of unsupervised representations for downstream tasks has historically lagged behind that of the representations coming from supervised training (Caron et al. 2018).

However, very recent progress in self-supervised learning has now closed the gap with supervised learning in computer vision (He et al. 2020; Chen, T. et al. 2020a; Chen, X. et al. 2020; Chen, T. et al. 2020b). Self-supervised methods learn representations by training models to solve contrived tasks (e.g., filling in empty regions of data samples, or identifying different versions of the same object as a pair) where the labels are generated algorithmically from an unlabeled dataset. The aim is to design models and tasks that yield semantically meaningful representations which are useful for a variety of downstream tasks, and can be directly used or fine-tuned for these applications. Self-supervised pre-training is vital to state-of-the-art natural language models (Devlin et al. 2019; Radford et al. 2018; Nayak 2019); now that this method has undoubtedly crossed over into the computer vision domain, it has exciting prospects for broad scientific use.

In this paper, we demonstrate that self-supervised learning indeed has great utility for large astronomical surveys, using ~ 1.2 million SDSS *ugriz* galaxy images with 64×64 pixels as a proof of concept dataset (full details of data acquisition and selection are given in Appendix A). In section 2, we review the method of contrastive self-supervised learning and propose data augmentations that induce good representations for sky survey images. This approach allows us to build powerful representations which we showcase in section 3.1. In sections 3.2 and 3.3 we use the self-supervised representations to quickly outperform supervised learning

at two very common downstream tasks: morphological classification and inference of photometric redshifts, respectively.

2. METHOD

Recent self-supervised works (Bachman et al. 2019; Goyal et al. 2019; He et al. 2020; Chen, T. et al. 2020a; Chen, X. et al. 2020; Chen, T. et al. 2020b) use contrastive losses (Hadsell et al. 2006) to minimize the distance between different *views* (augmentations) of the same image in a learned representation space, while maximizing the distance between the representations of different images. The randomized augmentations producing these views should be semantic-preserving transformations of the input images, and the goal is to make the final representation invariant to these transformations (Tian et al. 2020; Xiao et al. 2020). This key design choice is application-dependent and requires prior knowledge. For example, in a galaxy survey, changing colors of galaxies could be detrimental for the downstream task of inferring photometric redshifts, even though color augmentation may be useful when classifying cats and dogs. For a base set of image augmentations that would be useful to the vast majority of downstream applications in sky surveys we propose the following:

- **Galactic extinction.** We want features to be invariant to the galactic latitude and object’s position on the celestial sphere. To model the effects of foreground galactic dust, we introduce artificial reddening by sampling a $E(B - V)$ reddening value from $\mathcal{U}(0, 0.5)$ and applying the corresponding per-channel extinction according to the photometric calibration from Schlafly & Finkbeiner (2011).
- **Point Spread Function (PSF).** Due to a variety of factors over the time span of a galaxy survey, images do not have a consistent PSF. To be invariant to this we experiment with a PSF augmentation, modeled as wavelength-dependent Gaussian smoothing with a standard deviation in r -band drawn from $\mathcal{N}(0, 0.13'')$ and scaled appropriately to the other channels using $\lambda^{-0.3}$ (Xin et al. 2018).
- **Rotation.** To be invariant to the apparent orientation of each galaxy, we sample the angle of random rotation of each image from $\mathcal{U}(0, 2\pi)$.
- **Random jitter & crop.** We also desire invariance to the image centering. Thus, two integers are sampled from $\mathcal{U}(-7, 7)$ to move (jitter) the center of the image (of size 107^2) along each respective axis, then the jittered image is center-cropped to size 64^2 .
- **Gaussian noise.** Finally, to be invariant to the instrumental noise, we sample a scalar from $\mathcal{U}(1, 3)$ and

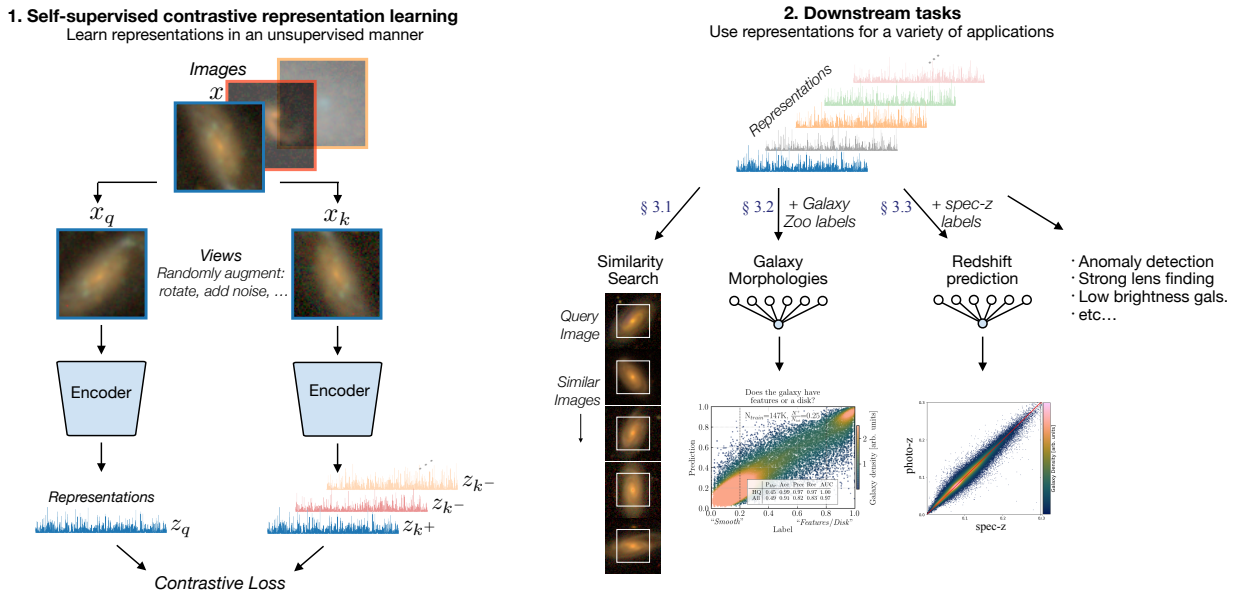


Figure 1. (Left) A schematic of the contrastive self-supervised framework. (Right) Examples of downstream tasks that can be learned on the learned representations.

multiply it with the aggregate median absolute deviation (MAD) of each channel (pre-computed over all training examples) to get a per-channel noise scale γ_c . Then, we introduce Gaussian noise sampled from $\mathcal{N}(0, \gamma_c)$ for each color channel.

The relative importance of these augmentations for producing good representations depends on both the dataset and the implementation of each augmentation. We evaluate representation quality by fine-tuning our representations for the task of redshift estimation under limited data labels (see Appendix C for details), finding Gaussian noise to be our strongest data augmentation and PSF the weakest, likely because pooling layers in our convolutional neural networks (CNNs) are robust to small-scale smearing. Best quality is achieved when we apply all augmentations except PSF. Note that these findings will not necessarily generalize to other surveys with different resolutions, signal-to-noise ratios, or target objects.

A schematic of the self-supervised pre-training framework used is shown in Figure 1 (Left). Applying our augmentations to samples \mathbf{x} , we get a pair of views that are denoted “positive” ($\mathbf{x}_q, \mathbf{x}_{k+}$) when the two come from different transformations of the same image, and “negative” ($\mathbf{x}_q, \mathbf{x}_{k-}$) otherwise. For each of the views, an encoder network extracts a 2048 dimensional representation $\mathbf{z} = \text{encoder}(\mathbf{x})$, and is trained to make positive pairs have similar representations while making negative pairs have dissimilar representations via a contrastive loss function:

$$L_{q, k^+, \{k^-\}} = -\log \left(\frac{\exp(\text{sim}(\mathbf{z}_q, \mathbf{z}_{k^+}))}{\exp(\text{sim}(\mathbf{z}_q, \mathbf{z}_{k^+})) + \sum_{k^-} \exp(\text{sim}(\mathbf{z}_q, \mathbf{z}_{k^-}))} \right), \quad (1)$$

where $\text{sim}(\mathbf{a}, \mathbf{b}) = \mathbf{a} \cdot \mathbf{b} / (\tau \|\mathbf{a}\| \|\mathbf{b}\|)$ is the cosine similarity measure between vectors \mathbf{a} and \mathbf{b} , normalized by a tunable “temperature” hyper-parameter τ . This loss (InfoNCE, Oord et al. 2018) is minimized when positive pairs have high similarity, while negative pairs have low similarity. We have closely followed Chen, X. et al. (2020) in our self-supervised learning setup, and more implementation details are given in Appendix D.

3. RESULTS

In our results, we demonstrate how the model has organized the image representation space. We explore how morphological characteristics from the Galaxy Zoo 2 project (GZ2, Willett et al. 2013) and spectroscopic redshifts from SDSS map onto this representation space. Then, using the labels from these two sources, we evaluate the utility of our self-supervised representations in actually performing the downstream tasks of morphology classification and photometric redshift estimation.

3.1. Self-supervised learning visualization

To visualize the information contained in the self-supervised representations we use Uniform Manifold Approximation and Projection (UMAP, McInnes et al. 2018) to reduce the 2048 dimensional representations

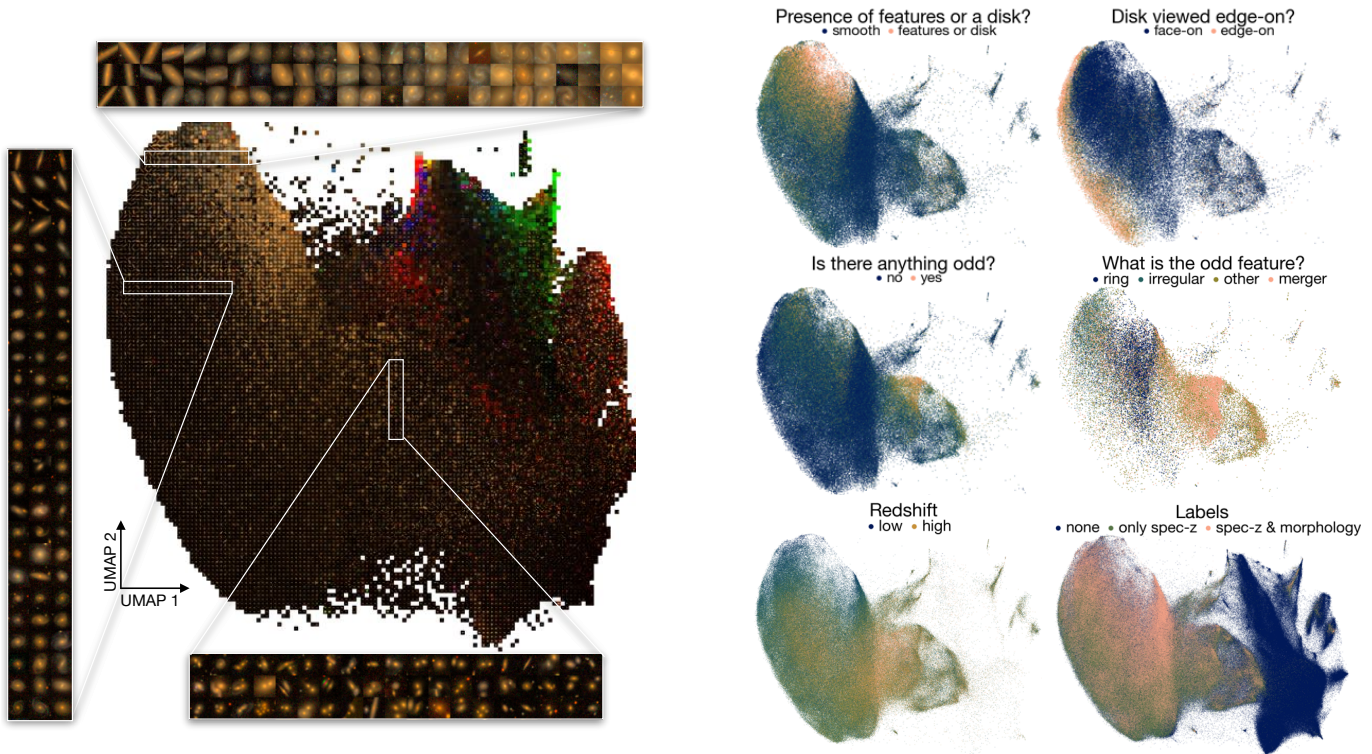


Figure 2. Visualizing the two dimensional UMAP projection of the self-supervised representations. The left panel shows randomly sampled representative images at each point in the space, while the right colors the space using answers to morphological classification questions from Galaxy Zoo 2, SDSS spectroscopic redshifts, or by labels.

to a more manageable 2, while preserving structure information on both local and global scales. We want to emphasize that although UMAP can produce meaningful clusters when trained directly on image data, we are using it here only for visualization purposes of the representation space. The fact that the morphological classification tasks described in the next section are achieved through only a linear transformation of the representations, with no fine-tuning, means that the galaxies are organized in a semantically meaningful way in the representation space.

In Figure 2 we investigate this 2D projection. The left panel was created by binning the space into 128×128 cells, randomly selecting a sample that resides within each cell, and plotting its corresponding rgb mapped galaxy image at that location³. Around the edges we show zoom-ins to a variety of hand-selected areas, in which it is clear that images are grouped by their visual similarity (e.g., spiral or not, edge-on or not, etc).

The following six panels color each point using the redshift and morphology labels, and confirm that clustering is not only along visual characteristics. Distinct

clusters as a function of morphological type and redshift are immediately apparent, to the level where decision boundaries for a number of GZ2 questions can be drawn by eye. Morphological labels are uncertain, so we illustrate them as continuous colors representing the fraction of votes for one answer over the other. Interestingly, we see that a large number of unlabeled samples are separated from any that have either redshift or morphology labels, but as we show below, using them for self-supervised learning still proves beneficial for the downstream tasks.

When displayed through an interactive data portal (e.g. Reis et al. 2021), such visualizations built upon self-supervised representations can be invaluable to the broader astronomical community.

3.2. Galaxy morphology classification

Morphological classification of galaxies into subclasses based on the presence of visual characteristics such as spiral arms, central bars, or odd features, is key in order to study galaxy formation and evolution. The GZ project (Lintott et al. 2008) has been fundamental in this endeavour by crowd-sourcing morphological classifications for a significant number of galaxies. GZ2 (Willett et al. 2013), the successor to GZ, is focused on more fine-grained features, and in total achieved morphologi-

³ rgb images are obtained by ‘luptonizing’ (Lupton et al. 2004) the *gri* photometric bands

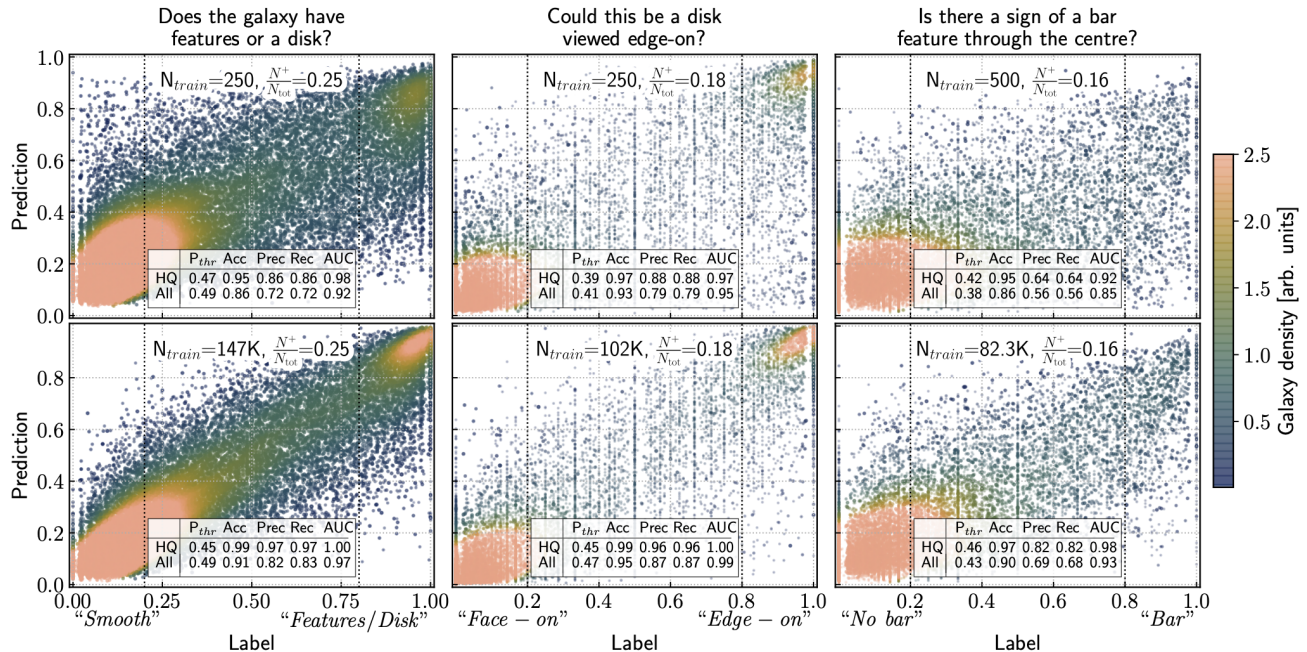


Figure 3. Predicted labels compared to crowd-sourced answers for three GZ2 questions. Top panels show the predictions on the test data when training with a highly limited number of labels, denoted by N_{train} , while the bottom panels show the predictions when using the full training set. We report the Accuracy, Precision, Recall, and AUC for “high quality” (HQ) labels (those with $P > 0.80$ or $P < 0.2$), and for all test samples. The level of class imbalance is reported by the fraction of positive training samples N^+/N_{tot} , and the size and opacity of the points is proportional to the number of crowd-sourced labels they received. Test sets for the three questions are of size (36,787, 25,531, 20,569) for “All” and (23,740, 20,452, 13,598) for HQ, respectively.

cal classifications of 304,122 SDSS galaxies. Shown most prominently by the winners of the “Galaxy Challenge” (Dieleman et al. 2015) and numerous subsequent works since (Domínguez Sánchez et al. 2018, 2019; Khan et al. 2019; Walmsley et al. 2020; Spindler et al. 2020; Vega-Ferrero et al. 2020), CNNs excel at this task.

Here, by treating each question as a separate classification task, we predict answers to the subset of GZ2 questions that are most commonly undertaken by ML methods. But, instead of training a CNN from scratch in a supervised setting, we simply train separate linear classifiers *directly on the self-supervised representations, with no fine tuning*. Each linear classifier requires only $\sim 0.5 - 10$ seconds on a GPU to train depending on the number of training samples used.

Figure 3 demonstrates the quality of the morphological predictions for three selected GZ2 questions, and shows the predicted label against the true label for a very limited number of training samples (top) and when using the full training set (bottom). We quantify the accuracy, precision, recall, and area under (AUC) the receiver operator characteristic curve in the inlaid tables (see Appendix B for definitions: 1.00 is the ideal value for all). Our results should be viewed most closely in relation to Domínguez Sánchez et al. (2018) and Walmsley et al. (2020), as both used SDSS images and focused on

GZ2 questions. “High Quality” labels (denoted HQ) are those with $P > 0.80$ or $P < 0.2$, while “All” includes every label for a given GZ2 question with at least 5 votes, regardless of the vote fraction for one answer over the other.

For the first two questions, ‘smooth or features/disk’ and ‘edge-on or face-on’, we find that only 50 training samples is sufficient to achieve high performance metrics on high quality samples. When increasing to larger training set sizes, the metrics quickly converge to the 100% or high 90% level for these questions. The ‘bar or no-bar’ question is the most difficult of the three due to uncertainty in human labelling, but accurate results are still achieved with limited training samples. We note that an exact quantitative comparison of our performance metrics to Domínguez Sánchez et al. (2018) and Walmsley et al. (2020) are not possible due to a lack of consistency in data sets, and in Appendix B we present our morphological results in more detail.

These results demonstrate that the self-supervised representations are extremely valuable for morphological classification. (1) They are essential to make accurate predictions when restricted by the number of available labels; (2) they improve accuracy metrics beyond what was achieved by pure supervised learning; (3) they provide avenues to investigate and isolate imaging artifacts

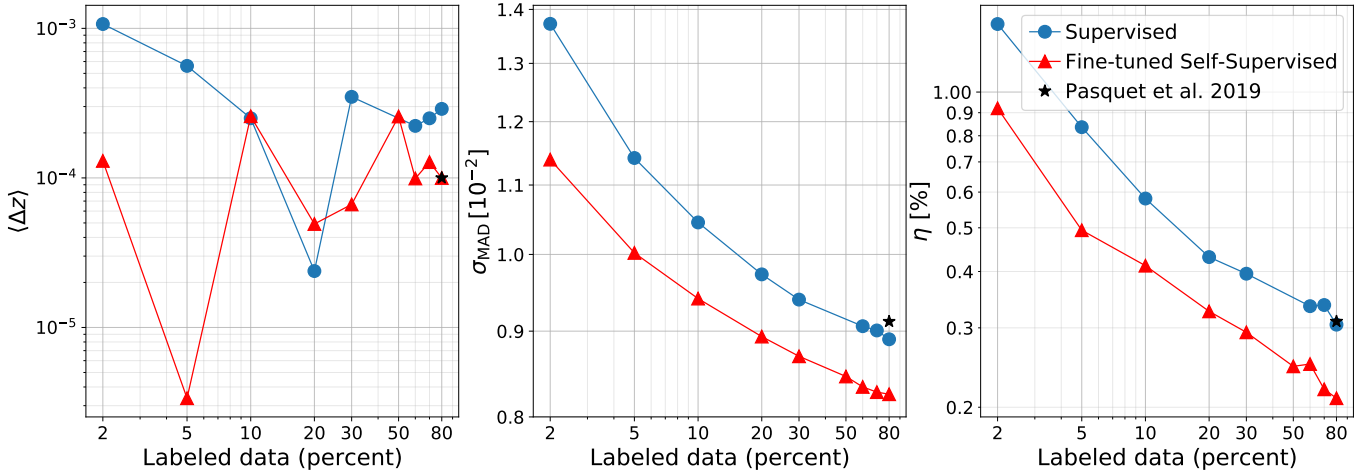


Figure 4. The prediction bias $\langle \Delta z \rangle$, dispersion σ_{MAD} , and outlier percentage η of photo- z estimates on test data, from our fine-tuned representations compared to reference fully-supervised networks. Trained on increasing fractions of the spec- z dataset, the fine-tuned self-supervised models perform best.

and anomalies as shown in the Appendix B, and (4) they can be used in pipelines to speed up crowd-sourced classification tasks: determine the next galaxy to be classified, perform a very computationally inexpensive similarity search⁴ to find N other similar galaxies, and classify them all at once.

3.3. Photometric Redshift Estimation

Determining the redshifts, and hence distances, to the billions of galaxies imaged in cosmological surveys is crucial to studying large-scale-structure, but taking high-precision spectroscopic redshift (spec- z) measurements for each galaxy is infeasible. Thus, a task of great importance to sky surveys is photometric redshift (photo- z) estimation (for a recent review, see Salvato et al. 2019). Photo- z models take multi-band galaxy photometry and use template fitting (Loh & Spillar 1986), machine learning (Connolly et al. 1995), or hybrid methods to produce estimates for the galaxy’s redshift z and its associated probability density function. Traditionally, such models relied on “hand-crafted” features extracted from the observations, but recent work has also successfully applied CNNs directly to the images themselves (Hoyle 2016; D’Isanto & Polsterer 2018; Pasquet et al. 2019). While promising, these supervised methods are inherently constrained by the limited size (and galaxy features, such as relative size or brightness) of the training dataset. Therefore, self-supervised representations derived from a larger body of unlabeled samples are a promising venue for improving accuracy and robustness.

⁴ we use faiss: <https://github.com/facebookresearch/faiss>

For easier comparison against established baselines on SDSS data, we closely follow the setup of Pasquet et al. (2019), whose CNN achieved significantly lower dispersion than previous image-based ML models. Their network is trained as a classifier over a discrete set of 180 redshift bins spanning $0 \leq z \leq 0.4$, where the photo- z estimate z_p is computed as the expectation $\mathbb{E}(z)$ over the probabilities predicted in each bin. We adapt this design into our ResNet50 model, and establish our own supervised baseline (with identical architecture as our self-supervised model) by training on the available spec- z labels. We use the following standard metrics to evaluate the accuracy of photo- z estimates:

- The prediction residual $\Delta z = (z_p - z_s)/(1 + z_s)$, where z_p and z_s correspond to the photometric and spectroscopic redshifts, respectively.
- The dispersion or MAD deviation, $\sigma_{\text{MAD}} = 1.4826 \times \text{MAD}(\Delta z)$, where $\text{MAD} = \text{median}(|\Delta z - \text{median}(\Delta z)|)$.
- η , the percent of “catastrophic” outliers with $|\Delta z| > 0.05$.

Results of our supervised training study are shown in the three left panels of Figure 4. As shown, we also test the improvement in the model accuracy as we increase the training dataset size. Similar to the results of Pasquet et al. (2019), the prediction bias $\langle \Delta z \rangle$ (a noise-dominated metric) is negligibly small, and our supervised baseline model matches the accuracy of Pasquet et al. (2019) in σ_{MAD} and η .

We then move to evaluating the utility of our self-supervised representations for photo- z estimation. To fine-tune them on the spec- z labels, we train a linear

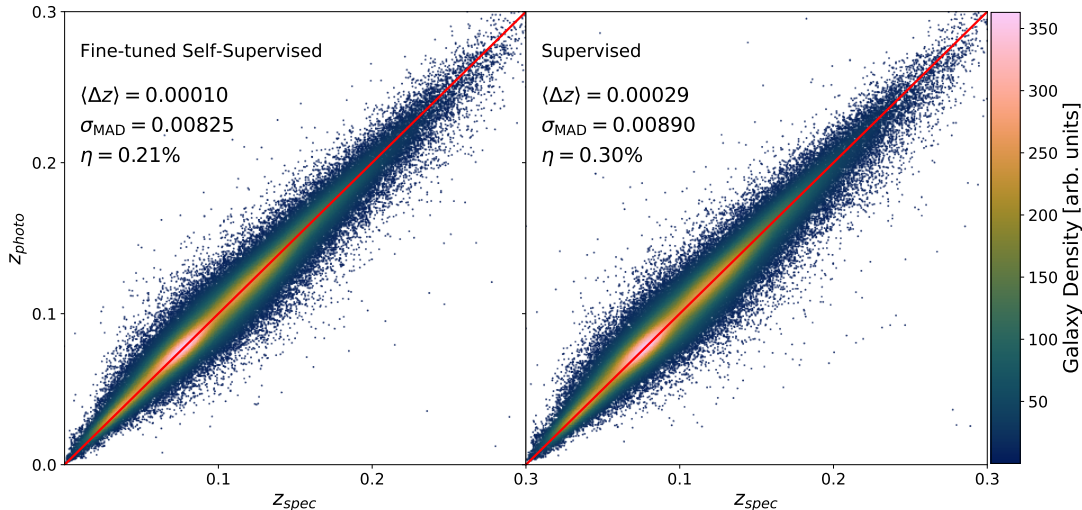


Figure 5. The photo- z estimates of our best model on test data, arising from fine-tuned self-supervised model (left), compared to the equivalent supervised network (right).

classifier on the representations while allowing the encoder weights to train with a $10\times$ smaller learning rate than that of the classifier (more fine-tuning details are in Appendix D). Results are shown in Figure 4.

At all fractions of training data used, the fine-tuned self-supervised representations achieve superior performance in σ_{MAD} and η compared to the equivalent supervised network. Impressively, the accuracy gained from pre-training on unlabeled data is equivalent to supervised training on $2 - 4\times$ more spec- z labels, with no modifications in architecture size or complexity. Consequently, our model, fine-tuned on the full training dataset, achieves a new state-of-the-art accuracy for CNN-based photo- z prediction on SDSS galaxies, as shown in Figure 5. This is an exciting result, as it suggests any existing supervised network developed for similar tasks on this type of data could get an immediate performance benefit from a self-supervised pre-training stage.

4. DISCUSSION AND CONCLUSIONS

In this letter we have demonstrated that self-supervised representation learning on unlabeled data yields notable performance gains over supervised learning for multiple tasks. These performance gains are achieved even when the self-supervised model is limited to have the same size as the baseline CNNs in downstream tasks. However, results from ML literature show that the best performance (i.e., the best representation quality) is achieved when self-supervised models are much larger (Radford et al. 2019; Chen, T. et al. 2020b). Thus, the possibility of training a large self-supervised model on massive photometry databases and “serving” the model for usage by the larger community,

much like the operation of existing state-of-the-art language models (Devlin et al. 2018; Radford et al. 2019), is an exciting new direction for ML applications in sky-surveys.

A major issue with all machine learning studies on labeled sky survey data is not just the limited size of the training data set, but also the selection bias imposed by gathering labels. For example, due to the series of flux and quality cuts applied when selecting spectroscopic targets (Strauss et al. 2002), galaxies with spec- z labels have a distinct bias towards nearby bright objects with low galactic extinction. Thus, galaxies selected for spectroscopic measurement are not representative of all those with photometry, as can clearly be seen in the representation space of Figure 2. Although ML methods can train on this labeled data and achieve a good test accuracy within this subset of galaxies, there are few robustness guarantees for photo- z estimation beyond the labeled distribution of galaxies. It has been shown, recently, that self-supervised pre-training (Hendrycks et al. 2019a,b) improves model robustness and uncertainty quantification, and that self-supervised models outperform their supervised counterparts in out-of-distribution detection on difficult outliers. This means self-supervised models have excellent prospects for mitigating distributional differences between (labeled) training and (unlabeled) inference data in sky surveys. We believe that self-supervised representation learning opens the door to leveraging the vast amounts of unlabeled, existing and future, sky survey data, promising a new era for ML applications in precision and discovery astrophysics.

ACKNOWLEDGMENTS

Authors would like to thank François Lanusse, Peter Melchoir, Evan Racah, and Edward Schlafly for helpful discussions. This research used resources of the National Energy Research Scientific Computing Center (NERSC), a U.S. Department of Energy Office of Science User Facility located at Lawrence Berkeley National Laboratory, operated under Contract No. DE-AC02-05CH11231. Md.H.'s work was supported by the NERSC's summer internship program. G.S. and Z.L. were partially supported by the DOE's Office of Advanced Scientific Computing Research and Office of High Energy Physics through the Scientific Discovery through Advanced Computing (SciDAC) program.

REFERENCES

- Alam, S., Albareti, F. D., Prieto, C. A., et al. 2015, *The Astrophysical Journal Supplement Series*, 219, 12
- Alloghani, M., Al-Jumeily, D., Mustafina, J., Hussain, A., & Aljaaf, A. J. 2020, *A Systematic Review on Supervised and Unsupervised Machine Learning Algorithms for Data Science* (Springer International Publishing), 3–21, doi: [10.1007/978-3-030-22475-2_1](https://doi.org/10.1007/978-3-030-22475-2_1)
- Bachman, P., Hjelm, R. D., & Buchwalter, W. 2019, in *Advances in Neural Information Processing Systems*, ed. H. Wallach, H. Larochelle, A. Beygelzimer, F. d'Alché-Buc, E. Fox, & R. Garnett, Vol. 32 (Curran Associates, Inc.), 15535–15545. <https://proceedings.neurips.cc/paper/2019/file/ddf354219aac374f1d40b7e760ee5bb7-Paper.pdf>
- Beck, R., Dobos, L., Budavári, T., Szalay, A. S., & Csabai, I. 2016, *MNRAS*, 460, 1371, doi: [10.1093/mnras/stw1009](https://doi.org/10.1093/mnras/stw1009)
- Caron, M., Bojanowski, P., Joulin, A., & Douze, M. 2018, arXiv e-prints, arXiv:1807.05520. <https://arxiv.org/abs/1807.05520>
- Cheng, T.-Y., Huertas-Company, M., Conselice, C. J., et al. 2020a, arXiv e-prints, arXiv:2009.11932. <https://arxiv.org/abs/2009.11932>
- Cheng, T.-Y., Li, N., Conselice, C. J., et al. 2020b, *MNRAS*, 494, 3750, doi: [10.1093/mnras/staa1015](https://doi.org/10.1093/mnras/staa1015)
- Chen, T., Kornblith, S., Norouzi, M., & Hinton, G. 2020a, arXiv preprint arXiv:2002.05709
- Chen, T., Kornblith, S., Swersky, K., Norouzi, M., & Hinton, G. 2020b, arXiv preprint arXiv:2006.10029
- Chen, X., Fan, H., Girshick, R., & He, K. 2020, arXiv preprint arXiv:2003.04297
- Connolly, A. J., Csabai, I., Szalay, A. S., et al. 1995, *Astronomical Journal*, 110, 2655, doi: [10.1086/117720](https://doi.org/10.1086/117720)
- Devlin, J., Chang, M.-W., Lee, K., & Toutanova, K. 2018, arXiv e-prints, arXiv:1810.04805. <https://arxiv.org/abs/1810.04805>
- Devlin, J., Chang, M.-W., Lee, K., & Toutanova, K. 2019, in *Proceedings of the 2019 Conference of the North American Chapter of the Association for Computational Linguistics: Human Language Technologies, Volume 1 (Long and Short Papers)* (Minneapolis, Minnesota: Association for Computational Linguistics), 4171–4186, doi: [10.18653/v1/N19-1423](https://doi.org/10.18653/v1/N19-1423)
- Dieleman, S., Willett, K. W., & Dambre, J. 2015, *MNRAS*, 450, 1441, doi: [10.1093/mnras/stv632](https://doi.org/10.1093/mnras/stv632)
- D'Isanto, A., & Polsterer, K. L. 2018, *A&A*, 609, A111, doi: [10.1051/0004-6361/201731326](https://doi.org/10.1051/0004-6361/201731326)
- Domínguez Sánchez, H., Huertas-Company, M., Bernardi, M., Tuccillo, D., & Fischer, J. L. 2018, *MNRAS*, 476, 3661, doi: [10.1093/mnras/sty338](https://doi.org/10.1093/mnras/sty338)
- Domínguez Sánchez, H., Huertas-Company, M., Bernardi, M., et al. 2019, *MNRAS*, 484, 93, doi: [10.1093/mnras/sty3497](https://doi.org/10.1093/mnras/sty3497)
- Fruchter, A. S., & Hook, R. N. 2002, *PASP*, 114, 144, doi: [10.1086/338393](https://doi.org/10.1086/338393)
- Goyal, P., Mahajan, D., Gupta, A., & Misra, I. 2019, in *2019 IEEE/CVF International Conference on Computer Vision (ICCV)*, 6390–6399, doi: [10.1109/ICCV.2019.00649](https://doi.org/10.1109/ICCV.2019.00649)
- Gunn, J. E., Carr, M., Rockosi, C., et al. 1998, *AJ*, 116, 3040, doi: [10.1086/300645](https://doi.org/10.1086/300645)
- Gunn, J. E., Siegmund, W. A., Mannery, E. J., et al. 2006, *AJ*, 131, 2332, doi: [10.1086/500975](https://doi.org/10.1086/500975)

- Hadsell, R., Chopra, S., & LeCun, Y. 2006, in 2006 IEEE Computer Society Conference on Computer Vision and Pattern Recognition (CVPR'06), Vol. 2, 1735–1742, doi: [10.1109/CVPR.2006.100](https://doi.org/10.1109/CVPR.2006.100)
- Hart, R. E., Bamford, S. P., Willett, K. W., et al. 2016, *Monthly Notices of the Royal Astronomical Society*, 461, 3663–3682, doi: [10.1093/mnras/stw1588](https://doi.org/10.1093/mnras/stw1588)
- He, K., Fan, H., Wu, Y., Xie, S., & Girshick, R. 2020, in *Proceedings of the IEEE/CVF Conference on Computer Vision and Pattern Recognition*, 9729–9738
- He, K., Zhang, X., Ren, S., & Sun, J. 2016, in *Proceedings of the IEEE conference on computer vision and pattern recognition*, 770–778
- Hendrycks, D., Lee, K., & Mazeika, M. 2019a, arXiv e-prints, arXiv:1901.09960. <https://arxiv.org/abs/1901.09960>
- Hendrycks, D., Mazeika, M., Kadavath, S., & Song, D. 2019b, arXiv e-prints, arXiv:1906.12340. <https://arxiv.org/abs/1906.12340>
- Hocking, A., Geach, J. E., Sun, Y., & Davey, N. 2018, *MNRAS*, 473, 1108, doi: [10.1093/mnras/stx2351](https://doi.org/10.1093/mnras/stx2351)
- Hoyle, B. 2016, *Astronomy and Computing*, 16, 34, doi: [10.1016/j.ascom.2016.03.006](https://doi.org/10.1016/j.ascom.2016.03.006)
- Ivezić, Ž., Connelly, A. J., Vanderplas, J. T., & Gray, A. 2019a, *Statistics, Data Mining, and Machine Learning in Astronomy* (Princeton University Press)
- Ivezić, Ž., Kahn, S. M., Tyson, J. A., et al. 2019b, *ApJ*, 873, 111, doi: [10.3847/1538-4357/ab042c](https://doi.org/10.3847/1538-4357/ab042c)
- Keel, W. C., Chojnowski, S. D., Bennert, V. N., et al. 2012, *MNRAS*, 420, 878, doi: [10.1111/j.1365-2966.2011.20101.x](https://doi.org/10.1111/j.1365-2966.2011.20101.x)
- Khan, A., Huerta, E. A., Wang, S., et al. 2019, *Physics Letters B*, 795, 248, doi: [10.1016/j.physletb.2019.06.009](https://doi.org/10.1016/j.physletb.2019.06.009)
- Laureijs, R., Amiaux, J., Arduini, S., et al. 2011, arXiv e-prints, arXiv:1110.3193. <https://arxiv.org/abs/1110.3193>
- Lintott, C., Masters, K., Simmons, B., Bamford, S., & Kaviraj, S. 2013, *Astronomy and Geophysics*, 54, 5.16, doi: [10.1093/astrophys/att162](https://doi.org/10.1093/astrophys/att162)
- Lintott, C. J., Schawinski, K., Slosar, A., et al. 2008, *MNRAS*, 389, 1179, doi: [10.1111/j.1365-2966.2008.13689.x](https://doi.org/10.1111/j.1365-2966.2008.13689.x)
- Lintott, C. J., Schawinski, K., Keel, W., et al. 2009, *MNRAS*, 399, 129, doi: [10.1111/j.1365-2966.2009.15299.x](https://doi.org/10.1111/j.1365-2966.2009.15299.x)
- Loh, E. D., & Spillar, E. J. 1986, *The Astrophysical Journal*, 303, 154, doi: [10.1086/164062](https://doi.org/10.1086/164062)
- Lupton, R., Blanton, M. R., Fekete, G., et al. 2004, *PASP*, 116, 133, doi: [10.1086/382245](https://doi.org/10.1086/382245)
- Margalef-Bentabol, B., Huertas-Company, M., Charnock, T., et al. 2020, *MNRAS*, 496, 2346, doi: [10.1093/mnras/staa1647](https://doi.org/10.1093/mnras/staa1647)
- Martin, G., Kaviraj, S., Hocking, A., Read, S. C., & Geach, J. E. 2020, *MNRAS*, 491, 1408, doi: [10.1093/mnras/stz3006](https://doi.org/10.1093/mnras/stz3006)
- McInnes, L., Healy, J., & Melville, J. 2018, arXiv e-prints, arXiv:1802.03426. <https://arxiv.org/abs/1802.03426>
- Nayak, P. 2019, "Understanding searches better than ever before". <https://blog.google/products/search/search-language-understanding-bert/>
- Oord, A. v. d., Li, Y., & Vinyals, O. 2018, arXiv preprint arXiv:1807.03748
- Pasquet, J., Bertin, E., Treyer, M., Arnouts, S., & Fouchez, D. 2019, *Astronomy & Astrophysics*, 621, A26
- Paszke, A., Gross, S., Massa, F., et al. 2019, in *Advances in Neural Information Processing Systems 32*, ed. H. Wallach, H. Larochelle, A. Beygelzimer, F. d'Alché-Buc, E. Fox, & R. Garnett (Curran Associates, Inc.), 8024–8035. <http://papers.neurips.cc/paper/9015-pytorch-an-imperative-style-high-performance-deep-learning-library.pdf>
- Radford, A., Narasimhan, K., Salimans, T., & Sutskever, I. 2018, *Improving language understanding by generative pre-training*
- Radford, A., Wu, J., Child, R., et al. 2019, *Language Models are Unsupervised Multitask Learners*
- Reis, I., Rotman, M., Poznanski, D., Prochaska, J., & Wolf, L. 2021, *Astronomy and Computing*, 34, 100437, doi: <https://doi.org/10.1016/j.ascom.2020.100437>
- Salvato, M., Ilbert, O., & Hoyle, B. 2019, *Nature Astronomy*, 3, 212
- Schlafly, E. F., & Finkbeiner, D. P. 2011, *The Astrophysical Journal*, 737, 103
- Spergel, D., Gehrels, N., Breckinridge, J., et al. 2013, arXiv e-prints, arXiv:1305.5422. <https://arxiv.org/abs/1305.5422>
- Spindler, A., Geach, J. E., & Smith, M. J. 2020, *MNRAS*, doi: [10.1093/mnras/staa3670](https://doi.org/10.1093/mnras/staa3670)
- Stein, G. 2020, *georgestein/ml-in-cosmology: Machine learning in cosmology, v1.0*, Zenodo, doi: [10.5281/zenodo.4024768](https://doi.org/10.5281/zenodo.4024768)
- Strauss, M. A., Weinberg, D. H., Lupton, R. H., et al. 2002, *AJ*, 124, 1810, doi: [10.1086/342343](https://doi.org/10.1086/342343)
- Tian, Y., Sun, C., Poole, B., et al. 2020, arXiv e-prints, arXiv:2005.10243. <https://arxiv.org/abs/2005.10243>
- Vega-Ferrero, J., Domínguez Sánchez, H., Bernardi, M., et al. 2020, arXiv e-prints, arXiv:2012.07858. <https://arxiv.org/abs/2012.07858>
- Walmsley, M., Smith, L., Lintott, C., et al. 2020, *MNRAS*, 491, 1554, doi: [10.1093/mnras/stz2816](https://doi.org/10.1093/mnras/stz2816)

- Willett, K. W., Lintott, C. J., Bamford, S. P., et al. 2013, MNRAS, 435, 2835, doi: [10.1093/mnras/stt1458](https://doi.org/10.1093/mnras/stt1458)
- Xiao, T., Wang, X., Efros, A. A., & Darrell, T. 2020, arXiv e-prints, arXiv:2008.05659.
<https://arxiv.org/abs/2008.05659>
- Xin, B., Ivezić, Ž., Lupton, R. H., et al. 2018, AJ, 156, 222, doi: [10.3847/1538-3881/aae316](https://doi.org/10.3847/1538-3881/aae316)
- Xiong, L., Poczos, B., Connolly, A., & Schneider, J. 2018, Anomaly Detection for Astronomical Data, Carnegie Mellon University, doi: <https://doi.org/10.1184/R1/6475475.v1>

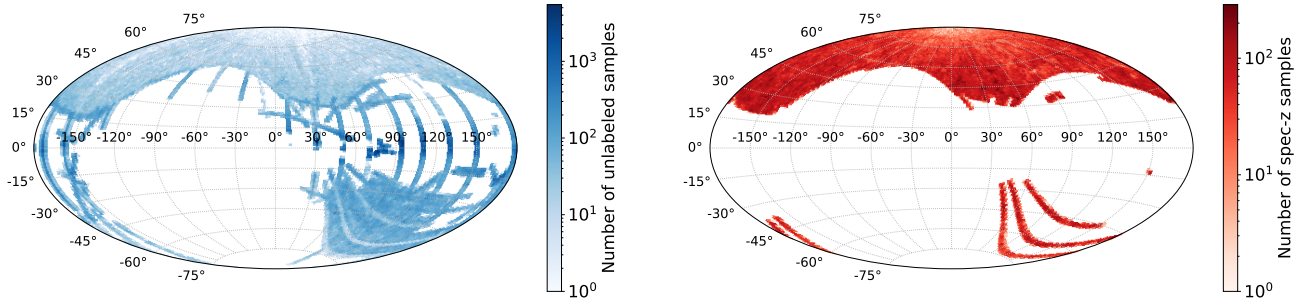


Figure 6. The spatial distribution of the full unlabeled (left) galaxy image dataset, and the spec-z labeled (right) dataset.

APPENDIX

A. DATASET DETAILS

Our database of galaxies is assembled from Data Release 12 (DR12; Alam et al. 2015) of the SDSS. To pull samples with spectroscopic redshift labels, we follow the process of Pasquet et al. (2019) in pulling from the Main Galaxy Sample to enable direct comparison to their results. Their SQL query filters for objects classified as ‘GALAXY’ with dereddened petrosian magnitudes $r \leq 17.8$ and spectroscopic redshifts $z \leq 0.4$. For us, the query returns 547,224 objects, and after removing some duplicates, we are left with 517,190 to use as labeled training examples. When fine-tuning our image representations for the photo- z estimation task, we use 400,000 images for training and 103,000 as validation dataset.

To build our larger set of galaxies with no spectroscopic labels, we filter for objects with dereddened petrosian magnitudes $r \leq 17.8$, on the ‘PhotoObjAll’ full photometric catalog of the SDSS. In the resulting set of galaxies, we remove duplicates which were already included in our spectroscopic sample, and exclude samples with an estimated photometric redshift (as estimated by Beck et al. (2016)) $z_{phot} > 0.8$. This eliminates objects which are too distant compared to the spectroscopic sample, but decreases the possibility that we are unnecessarily excluding samples whose true redshift is less than 0.4 (the cutoff for our spectroscopic sample) due to incorrect photo- z estimates. After imposing these cuts, we were able to successfully pull 845,254 objects. The spatial distributions of our labeled and unlabeled galaxy datasets are shown in Figure 6

SDSS photometric images contain data in 5 passbands ($ugriz$), and come background-subtracted but are not dereddened to account for galactic extinction. To pull images for our datasets, we use the Montage⁵ tool to query the imagery catalog in SDSS Data Release 9 (DR9), based on the tabulated equatorial coordinates for each object in our dataset. For each set of object coordinates, we sample a patch of sky of size $(0.012^\circ)^2$, centered on the object, and project onto a 2D image with 107^2 pixels (this ensures the resulting pixel scale is as close as possible to the native pixel scale in the SDSS, 0.396 arcsec). In each image, we store the u , g , r , i , and z passbands as 5 color channels.

The Montage pipeline uses Variable-Pixel Linear Reconstruction (Fruchter & Hook 2002) during the projection process to appropriately transform source input pixel values into the output pixel space. With this setup, a few samples were returned containing corrupted values at the edges of the image, so we crop all images to 107^2 pixels to eliminate such issues. Note that during training of the self-supervised model, we impose random rotations and random jitter to each image before cropping out the central portion as a data augmentation, so while our photometric images contain 107 pixels per side, the CNNs in this work only view samples of size 64^2 pixels. This input size of CNN is consistent with the photo- z CNN model of Pasquet et al. (2019).

⁵ <http://montage.ipac.caltech.edu/>

B. GALAXY MORPHOLOGY CLASSIFICATION

In Section 3.2 we displayed morphological predictions for a subset of Galaxy Zoo 2 (GZ2) labels. Here, we describe the training data and detail the training procedure for the linear classifier, and put in further context the accuracy of the predictions with respect to previous methods.

B.1. Training methodology

Galaxy Zoo 2 (Willett et al. 2013) achieved 16 million morphological classifications of 304,122 galaxies drawn from SDSS with $r < 17$ and $\text{petroR90.r}^6 > 3$ arcsec, collected via a web-based interface. For each galaxy users were shown a 424×424 pixel image scaled to 0.02 petroR90.r arcseconds per pixel, and were led down a multi-step decision tree to answer increasingly detailed questions about the visual appearance of the galaxy. For example, users were first asked “Is the galaxy simply smooth and rounded, with no sign of a disk?”, and had the option of selecting responses “smooth”, “features or disk”, or “star or artifact”. Their selection of a response is referred to as their *vote*. Based on their response to a question they are lead down different branches of the decision tree - if “smooth” was selected, they are next asked “how rounded is it”, but if “features or disk” was selected they will be asked a series of questions about spiral arms, bulge shapes, and a variety of other morphological features.

There are 11 total of these *classification tasks* (questions) that have the potential of being asked in the GZ2 decision tree, and the number of possible responses for each classification ranges from 2 to 7. We focus on binary tasks, with the exception of the first question where the response “star or artifact” occurs so infrequently (0.08% of responses select this as the majority) that it can be effectively neglected. All tasks beyond the first one depend on responses to previous tasks in the decision tree. For example, “could this be a disk viewed edge on?” is only asked if the user responded “features or disk” on the first task. Thus, a response for “edge-on” over “face-on” is not a binary classification of the total galaxy population, but only a sub-classification of galaxies that were already considered to have features or a disk.

The nature of data collection (non-expert labelled), coupled with the uncertain class boundaries for galaxies with faint features, result in individual GZ2 users voting for different answers, and therefore uncertain morphological classifications are given for each galaxy. We consider the “consensus weighted vote fractions” - the fraction of users who voted for an answer⁷ - as the true probability of a galaxy belonging to one class over the other, and we predict an equivalent class probability between (0, 1). Rather than a binary prediction, the returned probability represents the uncertainty of the morphology of the galaxy as seen in an SDSS image, whether this uncertainty stems from faint features, mislabelling, or imaging artifacts. Other works use the “de-biased estimate”, which estimates how the galaxy would have been classified if viewed at $z = 0.03$ (Hart et al. 2016). By using the consensus weighted fractions we estimate what the image actually shows, not the “true” morphology, and debiasing can be performed after prediction.

We use the GZ2 main sample with spectroscopic redshifts which includes morphological classifications for 243,500 galaxies. The main sample without photometric redshifts of 42,462 galaxies, and the stand-alone Stripe 82 catalogue of 17,787 galaxies, were not included. We cross match the GZ2 table⁸ with our SDSS database and search for pairs whose equatorial coordinates overlap within within 5 pixels (1.98 arcsec). This returns a final sample of 183,929 galaxies for which we have both *ugriz* images and crowd-sourced morphological classifications. This sample also contains redshift information which was used separately for photo-z prediction.

B.2. Network \mathcal{E} training

We predict the vote weighted user response by training a simple linear classifier on the self-supervised representations. The linear layer maps the 2048 dimensional representation to 1 dimension with 2048 trainable weights and one bias parameter, followed by a softmax function to ensure the probability is within the range (0, 1). Each GZ2 question has its own linear classifier, trained separately using the subset of galaxies that have at least five total votes for that question. Thus, the predicted probability should be interpreted as follows: regardless of the vote fraction of responses to previous questions, what is the consensus vote *of the users that ended up at this question on the decision tree*. If only 10% of users selected “features or a disk” for the first question, the galaxy most likely is smooth and does not

⁶ petroR90.r is the Petrosian radius which contains 90% of the r-band flux

⁷ consensus weighted fractions are slightly different than the true vote fraction, they are the result of re-weighting users votes based on their overall consensus with others who looked at the same image

⁸ Galaxy Zoo data is located at <https://data.galaxyzoo.org/>

have a disk. Yet we still use the vote fraction of that 10% of users that were then subsequently asked “could this be a disk viewed edge-on?” when training a classifier for the edge-on question. Classifiers can then be used in conjunction after training.

Training was conducted in PyTorch (Paszke et al. 2019) through a binary cross entropy loss on the soft labels (consensus weighted vote fractions). A random sample of 20% of the data was set aside for testing, and was not used for training any of the classifiers. Many questions have a high degree of class imbalance which reflects the occurrence of galaxy morphologies in the nearby universe. We found that balanced class weights (each instance of the class weighted by the overall occurrence fraction of that class) did not improve the classification performance. Optimization was performed using Limited-memory BFGS (LBFGS) and a learning rate of 0.01. K-fold cross validation was utilized with $k = 5$ by splitting the training dataset into k subsets, training on $k - 1$ of them, and using the last as a validation set in order to perform early stopping when the error on the validation set began to increase. Final predictions are then taken as an average over the 5 networks. K-fold cross-validation has no discernible improvement on the results, but was used as it can provide more robust predictions when training with a very small number of labels, and can provide some estimate of uncertainty on the prediction. For each linear classifier, training generally concluded within a few epochs and $\sim 0.5 - 10$ seconds of compute time on a GPU. Note that this does not take into account the compute time required to learn the self-supervised representations, which this is shared between all downstream tasks, and does not need to be undertaken for each one separately.

As evidenced by Figure 2, the self-supervised representations have achieved a high degree of separation between numerous types of galaxy morphologies. Likewise, we found that classification became a straightforward task when using any subset of the labels. Unlike DS+18, we found no need to separate uncertain labels from high probability ones. Limiting our training set to only ‘high quality’ (HQ) labels (those with $P < 0.2$ or $P > 0.8$), resulted in nearly equivalent performance on HQ labels in the test set, but decreased the performance on uncertain labels (those with $0.2 < P < 0.8$). We also found no need to impose higher minimum cuts on the number of votes (10) for some questions, as W+20 found was needed to improve classification performance from random initialization.

B.3. Performance metrics & additional results

Figure 3 demonstrated the quality of the morphological predictions for three selected GZ2 questions. To measure the performance of a binary classifier, we quantify the accuracy (Acc), Precision (Prec), recall or true positive rate (Rec/TPR), false positive rate (FPR), and area under (AUC) the receiver operator characteristic curve:

$$\begin{aligned} \text{Acc} &= \frac{\text{TP} + \text{TN}}{(\text{TP} + \text{FP}) + (\text{TN} + \text{FN})} \\ \text{Prec} &= \frac{\text{TP}}{\text{TN} + \text{FP}} \\ \text{Rec/TPR} &= \frac{\text{TP}}{\text{TP} + \text{FN}} \\ \text{FPR} &= \frac{\text{FP}}{\text{FP} + \text{TN}} \\ \text{AUC} &= \int \text{TPR}d(\text{FPR}), \end{aligned}$$

Where TP and TN are the number of true positives and true negatives, and FP and FN are the number of false positives and false negatives, respectively. Figure 7 shows these performance metrics in the style of DS+18 figure 4 and W+20 figure 9. The format of Figure 3 was instead displayed in the main text as it displays not just the averaged performance metrics, but illustrates the degree to which each galaxy has been classified correctly, given in some cases very uncertain labels.

We note that an exact quantitative comparison of our performance metrics to these works, or to other automated morphological classification works, is not possible due to a lack of consistency in data sets. The samples used from the full set of GZ2 answers are not consistent: images can be from different SDSS data releases and have inconsistent pixel sizes or number of pixels, they use different observation bands (we use 5 here, while most works use 3), and different GZ2 vote fraction definitions are used as the “ground truth” morphological classification. Most importantly, the class imbalance used in training/testing is significantly lower in our work, and more imbalanced datasets will more easily show up as higher metric scores. Nevertheless, the results achieved here are extremely promising, and show

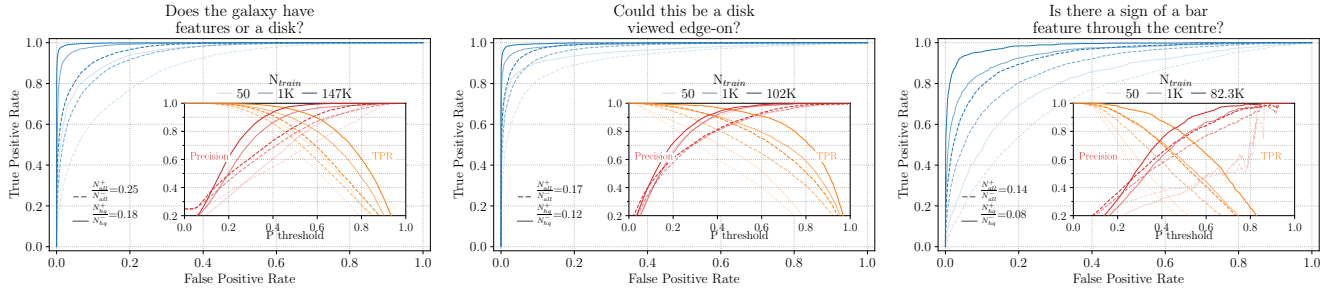


Figure 7. Binary classification results for the same three GZ2 questions of Figure 3, but displayed instead as ROC curves to more easily compare to Figures 4 and 9 from Domínguez Sánchez et al. (2018) and Walmsley et al. (2020), respectively. The Precision and TPR are shown as a function of a cut on the predicted probability. Three training set sizes are depicted by the opacity of a line, where training samples were chosen randomly without selecting clean high confidence subsets. Test sets for the three questions are of size (36787, 25531, 20569) for “All” and (23740, 20452, 13598) for HQ samples, respectively. Dashed lines show the metrics when applied to all test samples, while solid show when only compared to high quality labels.

that the use self-supervised representations allows us to push beyond the limits of supervised learning for automated morphological classifications.

Misclassified galaxies have three main failure modes which can be addressed in future work to further improve results beyond those achieved here. Firstly, our images span 25.3 arcseconds, which is not large enough to cover the entire angular extent of very nearby and large galaxies. In contrast, GZ2 participants were shown images scaled to ensure the entire galaxy was always visible, as do other automated classifications. Classifying these limited number of these galaxies is easily achievable by human means, so targeting these few samples is not of top priority. But, for the specific downstream task of classifying galaxy morphologies an additional augmentation which scales the angular extent of galaxies may prove beneficial. Second, a number of misclassified galaxies have imaging artifacts, which fine tuning the network would likely help improve the classification. A similarity search on the self-supervised representations provides a very valuable tool to isolate these artifacts. Finally, some ‘misclassified’ galaxies are the result of label uncertainty.

C. DATA AUGMENTATION ABLATION STUDY

In Section 2 we have listed a basic set of augmentations which make intuitive sense for use in a contrastive learning framework, as each augmentation is associated with some source of observational variability within the images that we want the learned representations to be invariant to. A relevant task in developing the self-supervised model is deciding which combinations of these augmentations are most effective in producing high-quality, semantically useful image representations. This can be answered in a number of ways, but is traditionally done in computer vision by taking a sample downstream task, like image classification, and training a linear classifier on top of the learned representations to perform it. Doing so evaluates the quality of the learned representations by measuring, e.g., how easily different classes are linearly separated in the representation space.

Such an approach is straightforward for the task of morphology classification, but is slightly ill-conceived for something more challenging like photo-z estimation, since the “classes” output by the network represent consecutive redshift bins which should not necessarily be linearly separable. Instead, we evaluate our representations by fine-tuning them for the photo-z estimation task and using the σ_{MAD} of predictions on test data as our quality metric. To ensure this metric is more closely tied to the representation quality rather than the supervised fine-tuning process, we only consider the performance of models which are fine-tuned on 10%, 20%, and 30% of the labeled data.

The results of our evaluation are shown in Figure 8. We find that on our dataset, the Gaussian noise augmentation seems to be the strongest, but that the best performance is achieved when we use all augmentations except the PSF smoothing. An important note here is that this finding depends both on our dataset as well as the way we have implemented each augmentation. Using contrastive learning with other surveys would require different implementations and possibly different augmentations, and could produce different “hierarchies” of augmentation strengths. In general, careful thought needs to be put into the data augmentations and which transformations one wants the representations to be invariant against (Xiao et al. 2020).

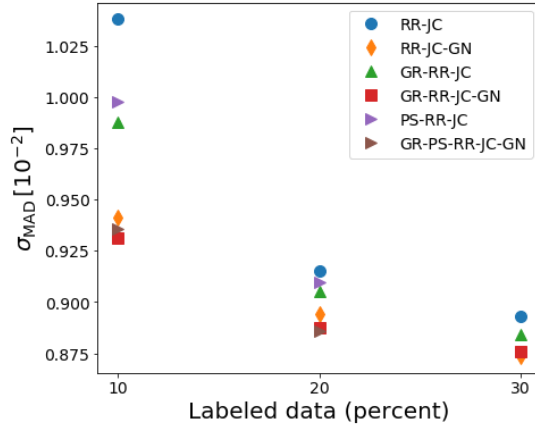


Figure 8. The σ_{MAD} of photo- z predictions from models fine-tuned on various fractions of the labeled data, showing how different combinations of augmentations affect downstream performance. Augmentations shown are random rotation (RR), jitter crop (JC), Gaussian noise (GN), galactic reddening (GR), and point spread function (PS).

D. ADDITIONAL ARCHITECTURE, HYPERPARAMETER, & TRAINING DETAILS

D.1. Self-supervised framework

Encoder: We follow (He et al. 2020; Chen, T. et al. 2020a) in using a ResNet50 architecture (He et al. 2016) as our encoder. Specifically, we use the implementation of the TorchVision library (`torchvision.models.resnet50`) which is a part of the PyTorch project (Paszke et al. 2019). The standard ResNet50, however, is designed to work on wider images than our 64×64 ones. To maintain reasonably wide representations by the end of the 50 layers, we change the first `Conv2d` layer to have `stride=1` instead of the default `stride=2`, we also remove the first `MaxPool2d` layer. This gives us $4\times$ wider activations throughout the network than what we would get with the defaults of ResNet50. The output of the `AdaptiveAvgPool2d` layer of the network is our representation, a 2048 dimensional vector. We also change the number of input channels to 5 to work with our 5 *ugriz* passbands data.

Following (Chen, T. et al. 2020a; Chen, X. et al. 2020), we don’t use the representation \mathbf{z} directly in the loss in Eq. 1, instead, we use a two layer MLP projection head which maps the representations to a space where the contrastive loss is applied. This has been shown to improve the learned representations. The output of the projection head is a 128 dimensional vector. The head is discarded after the self-supervised training process is completed.

Momentum encoder: In contrastive learning setups, in order to make the task of identifying positive examples non-trivial, it is crucial to have a large set of negative examples. For this we use the momentum encoder idea from (He et al. 2020); we maintain a queue of size 62K representations ($\sim 5\%$ of the training dataset size) that is continuously being updated during the training process. The representations in the queue are encoded using a momentum encoder; a second encoder with same architecture whose weights are an exponentially moving average of the main encoder weights. The parameters θ_k of the momentum encoder network are updated using the encoder parameters θ_q with momentum parameter m via

$$\theta_k \leftarrow m\theta_k + (1 - m)\theta_q. \quad (\text{D1})$$

The momentum hyper-parameter is set to $m = 0.999$. The momentum encoder helps maintain some consistency between the representations in the negative examples queue during the training. We use temperature parameter $\tau = 0.1$ in the contrastive loss.

During self-supervised pre-training, we use stochastic gradient descent with a cosine learning rate schedule, having an initial learning rate of 0.03. We pre-trained our network for 12 hours using 8 NVIDIA V100 GPUs on $\sim 1.2\text{M}$ images to complete ~ 50 epochs and this proved to be good enough for learning useful features used in this study. We have used `DistributedDataParallel` of PyTorch to leverage distributed training.

D.2. Photometric redshift estimation networks

We closely follow the setup of Pasquet et al. (2019), whose CNN is trained as a classifier over a discrete set of 180 redshift bins of size $\delta z = 2.2 \times 10^{-3}$ spanning $0 \leq z \leq 0.4$, where the photo- z estimate z_p is computed as the

expectation $\mathbb{E}(z)$ over the probabilities predicted in each bin. We train models from scratch to establish a baseline with the ResNet50 architecture (with the same modifications made for the self-supervised pre-training encoder, see D.1). During training, images are de-reddened by using the tabulated $E(B - V)$ value with the photometric calibration in Schlafly & Finkbeiner (2011), then augmented with random rotations, and random jitter & crop. Only de-reddening and cropping is applied at testing or evaluation.

For the fine-tuned networks, we take the pre-trained encoder and replace the projection head with a single MLP layer. Here, parameters up to `AdaptiveAvgPool2d` are initialized with the pre-trained weights and the MLP layer has random initialization. The whole network is then trained on labels, with the pre-trained weights having a learning rate of 0.0001, and the MLP classifier layer having a learning rate of 0.001. We train for 100 epochs and reduce the learning rate by a factor of 10 at 60, 90-th epochs. In all cases we have a batch size of 256.